Check for updates

Journal of the Optical Society of America B

OPTICAL PHYSICS

Finite-difference coupled-mode analysis of waveguide gratings and their optimization for single-mode DFB lasers

SHAYAN SAEIDI,[1,2,3,*] SINA AGHILI,[1,2,3] TUHIN PAUL,[4] BORIS ROSENSTEIN,[1] VALERY TOLSTIKHIN,[5] PIERRE BERINI,[1,2,4] AND KSENIA DOLGALEVA[1,2,4]

[1]School of Electrical Engineering and Computer Science, University of Ottawa, Ottawa, Ontario K1N 6N5, Canada
[2]Nexus for Quantum Technologies Institute, University of Ottawa, Ottawa, Ontario K1N 6N5, Canada
[3]KVector Dynamics, Ottawa, Ontario K2B8E1, Canada
[4]Department of Physics, University of Ottawa, Ottawa, Ontario K1N 6N5, Canada
[5]Intengent Inc., Ottawa, Ontario K2K2X3, Canada
*shayan.saeidi@kvectordynamics.com

Received 9 September 2024; revised 1 December 2024; accepted 3 January 2025; posted 3 January 2025; published 31 January 2025

This study presents a semi-numerical algorithm based on the coupled-mode theory combined with finite differencing to assess the performance of one-dimensional trapezoidal waveguide gratings, as well as arbitrarily shaped ones. Our approach not only surpasses traditional finite-difference time-domain (FDTD) and finite-element method (FEM) solvers in computational efficiency but also provides insightful information on DFB stack design by including partially confined radiative waves. We apply this method to investigate fifth-order trapezoidal waveguide gratings and optimize groove profiles in the context of a single-mode DFB laser, demonstrating its potential for rapid design and analysis in photonics applications.

https://doi.org/10.1364/JOSAB.541856

1. INTRODUCTION

Since their introduction, waveguide Bragg gratings (WBGs) have played a vital role in the development of active and passive photonic devices. WBGs function by selectively reflecting certain wavelengths of light in accordance with the grating's periodicity. Distributed-feedback (DFB) and distributed Bragg reflector (DBR) cavity lasers, grating couplers, and filters are just a few of their many applications in optical tele- and datacom, sensing, microwave photonics, and more [1–3].

Conventionally, the coupled-mode theory (CMT) was extensively employed to investigate the performance of WBGs because it provides an effective way to model light interaction in these gratings by emphasizing the coupling between waves propagating in opposite directions. In this method, both fundamental forward- and backward-propagating contra-guided waves were considered in the calculation of the coupling coefficient—an essential parameter for evaluating WBG efficiency [4,5]. Streifer *et al*. significantly improved upon the CMT by incorporating all interacting waves, including guided modes, partially confined radiative modes (also termed partial waves), and diffracted waves [6]. Streifer's method was superseded by the numerical methods, which facilitate the modeling of WBGs with arbitrary-shaped corrugations [7–9]. However, the primary challenge associated with numerical methods is the long simulation time required, resulting in high computational expense.

Here, we report a newly developed semi-numerical algorithm to calculate the coupling coefficient of any arbitrary grating, resting on the CMT formulation introduced by Streifer *et al.* [6]. Our algorithm yields precise solutions for geometries of greater complexity than those examined by Streifer while requiring minimal computational resources, yielding results in significantly reduced computational time compared to mainstream numerical methods. The numerical algorithm is implemented in Python and available in Ref. [10].

The remaining of the paper is organized as follows. In Section 2, we present three methodologies for determining the coupling coefficient of a WBG: (A) the approach proposed and used in this paper, termed the finite-difference coupled-mode theory (FD CMT); (B) a numerical scheme based on the finite-element method (FEM); and (C) that using the finite-difference time-domain (FDTD) method. Subsequently, a comparative analysis of the results is reported in Section 3. In Section 4, we analyze a fifth-order grating, explain the rationale for this choice, and discuss the optimization of the WBG profile for single-mode operation in a DFB laser (DFBL). Finally, a conclusion is given in Section 5.

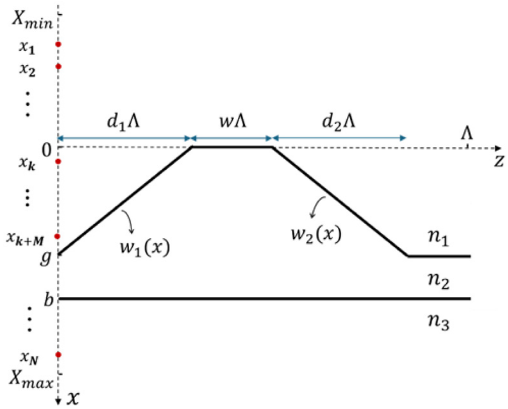

Fig. 1. Single period of the studied grating structure.

2. METHODS

A. Finite-Difference Coupled-Mode Theory

1. Finite-Difference Solution for Fundamental and Partial Waves

Figure 1 shows a three-layer slab waveguide featuring an embedded grating at the interface between its core and cover layers. In the real waveguide structure, it could be related to, the embedded WBG would be formed by patterned etching and blanket overgrowth, a standard process used in fabrication of the DFBLs, allowing for a certain degree of flexibility in terms of the grating pitch, shape, and depth.

Referring to the near-infrared spectral range, e.g., communication O- or C-band important for applications, the first-order grating would require such a lithography with well below 100 nm resolution, which is not commonly available in the photonic fabs. An alternative would be the higher-order grating, typically third or fifth order (depending on the etching process), implementable with a more accessible I-line stepper (365 nm wavelength).

Following Streifer's notation, the main transverse electric field component of the fundamental TE mode $\varepsilon_0(x)$ at the Bragg wavelength $\lambda_B = 2n_{\text{eff}}\Lambda$ is described by the Helmholtz equation:

$$\frac{d^2\varepsilon_0(x)}{dx^2} + \left[k_0{}^2 n^2(x) - \beta_0{}^2\right]\varepsilon_0(x) = 0, \tag{1}$$

where $k_0 = 2\pi/\lambda_B$ is the free-space wavenumber, $\beta_0 = 2\pi n_{\text{eff}}/\lambda_B$ is the propagation constant of the TE mode, and n_{eff} is its effective index. For the remainder of this paper, we will follow the time-harmonic form $\exp(-j\omega t)$ and consider only the TE mode.

The refractive index $n(x)$ equals n_1, n_2, and n_3 in the cover ($x < 0$), core ($g < x < b$), and substrate ($x > b$) regions, respectively. In the grating region ($0 < x < g$), the refractive index varies with both x and z. However, due to its periodicity in z, the z dependence can be expressed through a Fourier series, reducing the refractive index to a function of x alone. The details of this approach are provided in Ref. [6]. Therefore, in the grating region, the refractive index $n(x)$ is represented as

$$n_g(x) = \sqrt{n_2{}^2 + \frac{\left(n_1{}^2 - n_2{}^2\right)\left[w_2(x) - w_1(x)\right]}{\Lambda}}, \tag{2}$$

where the groove's profile is characterized by the functions $w_1(x)$ and $w_2(x)$, which are, in general, arbitrary. In this paper, we assume these functions to be linear, resulting in a trapezoidal profile. This choice allows for direct comparison with the results reported by Streifer *et al.* [11] and better aligns with DFB laser fabrication methods, as etching processes often produce grooves with linearly sloped walls.

To calculate the effective index of the waveguide with grating, n_{eff}, we employ a method similar to that described in Ref. [12]. We first discretize the grating region into a series of grids along the x axis. Figure 2(a) illustrates the 1D refractive index profile of the structure along the x axis (green lines), where according to Eq. (2), $n_g{}^2(x)$ varies linearly in the grating region ($0 < x < g$). We discretize the refractive index distribution $n_g{}^2(x)$ into M + 1 (M is an integer) equally spaced grids. The divisions between grids are identified by black dots in Fig. 2(a), each located at x_{k+v} ($v = 1, 2, \ldots, M$). At each division point, two distinct slab waveguides are constructed. An example for $x = x_{k+v}$ is shown in Fig. 2(a): the first waveguide (shown by red lines) incorporates the cover layer extending into the grating region with a thickness x_{k+v}. Beyond this point, another layer extends continuously to the core with the refractive index of $n(x_{k+v})$. The second waveguide (shown by blue lines) includes the core layer extending into the grating region with a thickness of $g - x_{k+v}$. Another layer extends from $x = x_{k+v}$ to the cover at $x = 0$, with the refractive index of $n(x_{k+v})$.

It is straightforward to calculate the effective refractive index of each slab waveguide, as described, e.g., in Ref. [13]. Figure 2(b) shows the effective index of these two waveguides (red and blue curves) as a function of x_{k+v} for grating System 1, described in Table 1. The n_{eff} of grating System 1 is taken as the average of these values and is found to be 3.5797, which shows excellent agreement with Ref. [11]. We used intervals of $x_{k+v} - x_{k+v-1} = 10$ nm in this calculation. Smaller intervals yield more accurate results but increase computation time. It is crucial to choose intervals small enough for n_{eff} to converge, as inaccurate values can significantly impact subsequent calculations.

After finding n_{eff} and β_0, the mode functions are expressed analytically within each layer. The first-order perturbation for the partial wave $\varepsilon_m(x)$ is defined by the solution of this equation [6,11]:

$$\frac{d^2\varepsilon_m^{(i)}(x)}{dx^2} + \left[k_0{}^2 n^2(x) - \beta_m{}^2\right]\varepsilon_m^{(i)}(x) = -k_0{}^2 A_{m-i}(x)\,\varepsilon_0(x), \tag{3}$$

where $\beta_m = \beta_0 + 2\pi m/\Lambda$ represents the propagation constant of the partial wave of order $m (m \neq i)$; $A_q(x)$ is the qth Fourier coefficient of the grating; and i denotes the forward ($i = 0$) or backward ($i = p$) propagation direction of the wave, with $p = -P$, where P is the grating order. $A_q(x)$ is zero everywhere except for the grating layer, where it equals

$$A_q(x) = \frac{n_f{}^2 - n_c{}^2}{j2\pi q}\left[e^{-\frac{j2\pi q w_2(x)}{\Lambda}} - e^{-\frac{j2\pi q w_1(x)}{\Lambda}}\right]. \tag{4}$$

Since Eq. (3) represents an inhomogeneous Helmholtz equation, numerical methods are preferable for its solution, especially for arbitrarily shaped grating profiles. Using our discretization of the structure along the x axis, we

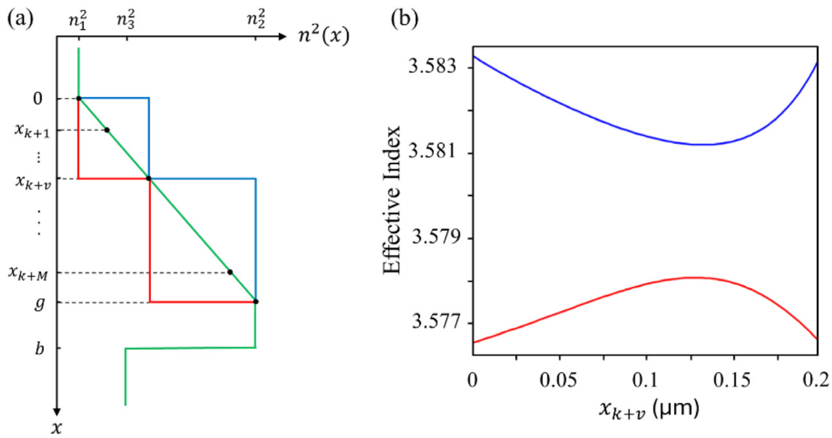

Fig. 2. (a) Refractive index distribution over the x axis, shown by the green lines. The grating layer is discretized into $M+1$ grids, where the division of grids is identified by black dots at x_{k+v} for $v = 1, \ldots, M$. Two waveguides are generated at each dot, shown by the red and blue lines. (b) Effective index of the waveguides depicted by the red and blue lines in (a), as a function of x_{k+v}.

Table 1. Parameters of the Grating System 1

Parameter	w	d_1	d_2	n_1	n_2	n_3	g	b	Λ	λ_B
Value	0	0.25	0.75	3.4	3.6	3.4	0.2 μm	1 μm	237.5 nm	850 nm

rewrite the left-hand side of Eq. (3) using a central difference approximation:

$$\varepsilon_m^{(i)''}(x) \approx \frac{\varepsilon_m^{(i)}(x+h) - 2\varepsilon_m^{(i)}(x) + \varepsilon_m^{(i)}(x-h)}{h^2}, \tag{5}$$

where

$$h = \frac{X_{\max} - X_{\min}}{N-1}. \tag{6}$$

Here, N is the total number of grids used in the discretization, and $X_{\min}$ and $X_{\max}$ are the boundaries of the simulation window. Thus, we transform the differential equation given by Eq. (3) into N linear equations of the form

$$\frac{\varepsilon^{(i)}_{m\ l+1} - 2\varepsilon^{(i)}_{m\ l} + \varepsilon^{(i)}_{m\ l-1}}{h^2} + \left(k_0{}^2 n^2(x_l) - \beta_m{}^2\right)\varepsilon^{(i)}_{m\ l}$$
$$= -k_0{}^2 A_{m-i}(x_l)\,\varepsilon_0(x_l), \tag{7}$$

where $1 \le l \le N$ (x_ls are shown in Fig. 1). There are N equations with $N+2$ unknowns, including $\varepsilon^{(i)}_{m\ 0}$ and $\varepsilon^{(i)}_{m\ N+1}$, which can be eliminated by substituting appropriate boundary conditions to terminate the computational domain at $X_{\min}$ and $X_{\max}$.

Given our emphasis on modeling partial waves (radiative modes), we apply radiative boundary conditions at $X_{\min}$ and $X_{\max}$ by defining plane waves propagating outward from the domain in the $\pm x$ directions at these locations. These conditions provide two additional equations, which allow us to relate $\varepsilon^{(i)}_{m\ 0}$ and $\varepsilon^{(i)}_{m\ N+1}$ to the fields within the domain. The radiative boundary conditions are defined as follows:

$$\varepsilon^{(i)}_{m\ 1} = \varepsilon^{(i)}_{m\ 0} e^{-jk_1 h}, \tag{8a}$$

$$\varepsilon^{(i)}_{m\ N} = \varepsilon^{(i)}_{m\ N+1} e^{-jk_N h}, \tag{8b}$$

where $k_1 = \sqrt{k_0{}^2 n_1{}^2 - \beta_m{}^2}$ and $k_N = \sqrt{k_0{}^2 n_3{}^2 - \beta_m{}^2}$ are the transverse components of the plane waves' wavenumbers.

2. *Computing Streifer's Coefficients*

Once the $\varepsilon_m^{(i)}$ are determined, the partial wave parameters $\zeta_{1,\ldots,4}$ introduced by Streifer *et al*. [6] can be readily calculated. These parameters, extensively discussed in Refs. [6,11], are summarized as follows:

$$\zeta_1 = \sum_{\substack{q=-\infty \\ q\neq 0,-p}}^{\infty} \eta^{(0)}_{q,-q}, \tag{9a}$$

$$\zeta_2 = \sum_{\substack{q=-\infty \\ q\neq 0,-p}}^{\infty} \eta^{(p)}_{q,-q}, \tag{9b}$$

$$\zeta_3 = \sum_{\substack{q=-\infty \\ q\neq 0,p}}^{\infty} \eta^{(p)}_{q,p-q}, \tag{9c}$$

$$\zeta_4 = \sum_{\substack{q=-\infty \\ q\neq 0,p}}^{\infty} \eta^{(0)}_{q,p-q}, \tag{9d}$$

where

$$\eta^{(i)}_{r,s} = \frac{k_0{}^2}{2\beta} \frac{\int_0^g A_r(x)\,\varepsilon_0(x)\,\varepsilon_s^{(i)}(x)\,\mathrm{d}x}{\int_{-\infty}^{\infty} \varepsilon_0{}^2(x)\,\mathrm{d}x}, \tag{9e}$$

$$\kappa_p = \frac{k_0{}^2}{2\beta} \frac{\int_0^g A_p(x)\,\varepsilon_0{}^2(x)\,\mathrm{d}x}{\int_{-\infty}^{\infty} \varepsilon_0{}^2(x)\,\mathrm{d}x}. \tag{9f}$$

Here κ_p is the coupling coefficient. In general, including more partial terms improves the accuracy of the results, though at the cost of increased computational time. However, per our experience, the partial terms have negligible effect when $|q| > P$ ($q \neq 0$). The coupling coefficient of the higher-order grating, incorporating contributions from partial terms $\zeta_{1,\ldots,4}$, can be

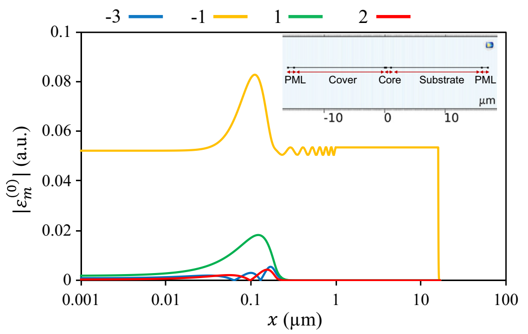

Fig. 3. Dominant orders of partial waves (legends show the order m). The inset presents the geometry of System 1, rigorously discretized by the FEM solver.

described using an effective coupling coefficient [14]:

$$\kappa_{\text{eff}} = \sqrt{(\kappa_p{}^* + \zeta_2)(\kappa_p + \zeta_4)}. \tag{10}$$

B. Finite-Element Method

We use the commercial FEM software, COMSOL v6.1 [15], to analyze an example triangular-profiled grating, labeled System 1 and described in Table 1. FEM solvers enable numerical calculations of n_{eff}, $\varepsilon_0(x)$, and $\varepsilon_m^{(i)}(x)$ through a multistep modeling process.

First, a wave equation study using the RF module is implemented to solve Eq. (1) numerically. The refractive indices and geometrical parameters of a WBG aligned with System 1 are defined. The inset of Fig. 3 shows the 1D configuration of the system as defined in the Geometry section of COMSOL. The simulation box is large enough and surrounded by perfectly matched layer (PML) boundary conditions to prevent reflections from the walls. Using the computed values of n_{eff} and $\varepsilon_0(x)$, we implement a general type of partial differential equation (PDE) from the Mathematics module,

$$\nabla \cdot \left(-c\nabla\varepsilon_m^{(i)}(x)\right) + a\varepsilon_m^{(i)}(x) = f, \tag{11}$$

to numerically calculate the partial waves. Equation (11) is defined by

$$c = -1/S(x), \tag{12}$$

$$a = \left(\beta_0^2 - \beta_m^2\right) S(x), \tag{13}$$

$$f = -k_0^2 A_{m-i}(x)\,\varepsilon_0(x)\,S(x), \tag{14}$$

where c, a, and f are the diffusion coefficient, the absorption coefficient, and the source term, respectively. The PML correction factor is

$$S(x) = 1 + i\frac{\sigma(x)}{\sqrt{|\beta_0^2 - \beta_m^2|}}, \tag{15}$$

where $\sigma(x)$ is the stretching factor [16].

Figure 3 shows the E-field distribution of the dominant orders of partially radiative waves across the waveguide in the forward setup ($i = 0$). The sudden drop of the fields at 15 µm is due to enforcing PML boundaries. It is obvious that the partial waves can constructively or destructively interact with guided modes while decaying as they approach the modified absorber walls. At the end of this step, one can recall Eqs. (9) and (10) to calculate the effective coupling coefficient of System 1.

C. Finite-Difference Time-Domain

Due to the periodic modulation in gratings, a range of wavelengths surrounding the Bragg wavelength λ_B will not be transmitted at the output of the gratings. This range is termed the stopband, and its width is referred to as the bandwidth. The bandwidth of a grating can be theoretically obtained using the CMT as [17]

$$\Delta\lambda = \frac{\lambda_B{}^2}{L n_{\text{group}}}\sqrt{1 + \left(\frac{L\,|\kappa_{\text{eff}}|}{\pi}\right)^2}, \tag{16}$$

where n_{group} represents the group index. According to Eq. (16), we can calculate the coupling coefficient by knowing the bandwidth.

One can utilize the FDTD technique to carry out this calculation. By modeling a finite-length grating bounded by PML conditions and launching the fundamental mode of the unperturbed waveguide at the input of the grating, the reflectance and transmittance of the waveguide mode can be computed. This is achieved by implementing frequency-domain monitors located at the input and output of the grating, respectively. Such simulations have been elaborated [18,19].

However, simulations of finite-length gratings are computationally expensive and time-consuming. A more efficient FDTD approach has been reported [20], wherein an infinitely long grating is modeled by simulating only one unit cell and applying Bloch boundary conditions along the propagation axis. We use this technique in the commercial software Lumerical FDTD [21] to determine $\Delta\lambda$ and subsequently calculate $|\kappa_{\text{eff}}|$ using Eq. (16). The fundamental mode of the slab waveguide serves as the source for our simulations. A mode pulse of a few femtoseconds (consecutively, with a broad spectrum) is launched into the grating. This pulse propagates to the output boundary, and due to the periodicity of the system, re-enters from the input boundary. This process repeats until the simulation time finishes or the energy within the simulation window reaches a predefined threshold. A frequency-domain monitor, positioned perpendicularly to the propagation direction within the simulation window, captures the wave spectrum transmitted through the system. The normalized square of the transmitted field, or transmittance, is illustrated in Fig. 4 for the grating System 1 for various simulation durations. It is evident that as the simulation time increases, the width of the peaks narrows, and the peaks become more distinguishable. Weak gratings have narrow bandwidths, and their peaks are closer to each other, therefore requiring more simulation time.

The bandwidth and the Bragg wavelength can be determined from the positions of these two peaks. By reformulating Eq. (16) with the length approaching infinity, the magnitude of the coupling coefficient can be deduced from

$$|\kappa_{\text{eff}}| = \frac{\Delta\lambda\pi\, n_{\text{group}}}{\lambda_B{}^2}. \tag{17}$$

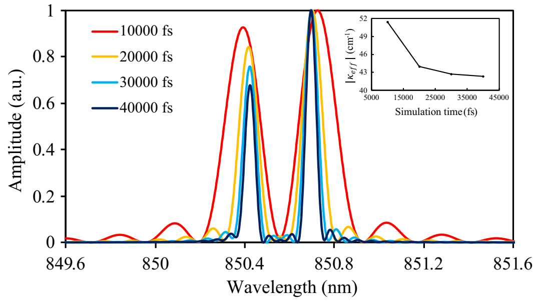

Fig. 4. Transmittance for different simulation times (from Lumerical FDTD). The inset shows calculated $|\kappa_{\text{eff}}|$ as a function of the simulation time.

The inset of Fig. 4 plots the variation of $|\kappa_{\text{eff}}|$ as a function of the simulation time. For materials with the refractive indices that are weakly dependent on the wavelength (such as III–V semiconductors in the infrared), n_{group} can be replaced by n_{eff} (as was done in this calculation). The convergence becomes evident with increasing simulation time, suggesting that short simulation times may yield inaccurate results.

3. COMPARISON OF METHODS

In this section, the coupling coefficients of the fundamental mode obtained by FD CMT, FEM, and FDTD are compared to each other and to the data reported in Ref. [13] for the grating structure of System 1, as a function of d_1 ($d_2 = 1 - d_1$). In FDTD simulations, we used 40,000 fs for the simulation time with a time step of 0.015 fs and a uniform mesh size of 3 nm. The FD CMT and FEM simulations were conducted with $-8 < q < 7$ and a mesh size of 3 nm for discretization. This mesh size was selected to ensure the convergence, as discussed later in this section.

Figures 5(a) and 5(b) plot $|\kappa_{\text{eff}}|$ and $\angle\kappa_{\text{eff}}$, respectively, as functions of d_1. Overall, good agreement exists between all three methods. The $|\kappa_{\text{eff}}|$ is minimum when the grating is symmetric and reaches its maximum at $d_1 = 0.15$ and 0.85. This triangled grating exhibits a small phase regardless of d_1, suggesting minimal radiation loss. The highest phase is achieved where $|\kappa_{\text{eff}}|$ is minimum. An important feature of a grating having a large phase of κ_{eff} is its ability to increase mode selectivity. This aspect will be discussed further in Section 4.

Table 2 compares the computational times of the three methods for the grating System 1. The computational power remains consistent across all cases, on an Intel Core i7-10700 CPU at 2.9 GHz processor and 32 GB of RAM. The efficiency of the FD CMT compared to other methods is remarkable.

Table 2. Comparison of Computing Time of Different Simulation Methods

Method	FD CMT	FEM	FDTD
Computing time (s)	∼10	∼900	∼600

The primary reason for the FD CMT's superior efficiency over the FEM lies in how each solver handles meshing. The FD CMT applies boundary conditions primarily at the edges of the overall problem domain to enforce physical constraints. In contrast, the FEM discretizes problem by thousands of free triangular elements, solving the solution within each element and ensuring convergence via regular iterative refinement. Meanwhile, the FDTD, being an inherently time-domain solver, requires both spatial and temporal stepping, which makes it a time-consuming method.

For the FEM, note that the actual simulation time is significantly longer than the listed computational time due to the need for identical data mapping between different modules in COMSOL.

Figure 6(a) illustrates the convergence of $|\kappa_{\text{eff}}|$ for each method as the mesh size is reduced from 45 nm. The FDTD method decreases in steps of 3 nm, while the FEM method is refined in steps of 10 nm. The FD CMT method is shown with continuous lines refined in 1 nm steps. Other simulation settings are as discussed above. In the smaller mesh size range (down to 10 nm), all the methods converge to the same value. However, as the mesh grid size increases, both the FDTD and FD CMT methods yield similar results due to their identical meshing principles along with a decrease in the simulation time. In contrast, the FEM shows better overall convergence owing to the higher accuracy of finite-element meshing, albeit at the cost of longer simulation times.

Figure 6(b) shows the convergence of $|\kappa_{\text{eff}}|$ as a function of the number of partial modes included in the FD CMT simulation. The partial modes, represented on the horizontal axis, are symmetrically distributed with respect to $q = 0$, excluding $q = 0$ itself. For example, including two modes corresponds to q ranging from -1 to 1. A value of 0 on the horizontal axis indicates that no partial mode is included. As discussed in Section 2.A.2, $|\kappa_{\text{eff}}|$ converges when the summations in Eq. (9) incorporate partial waves for $|q| > P$ (here, $P = 2$).

4. OPTIMIZATION OF THE WBG FOR A SINGLE-MODE DFBL

In the DFBL design, commonly used first-order gratings have the advantage that guided waves are decoupled from partial

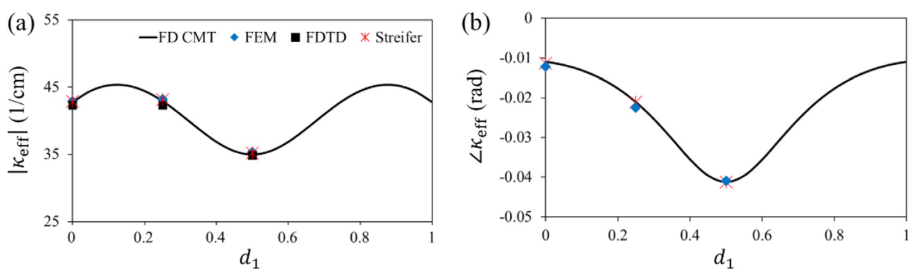

Fig. 5. Comparison of the (a) amplitude and (b) phase of the effective coupling coefficient κ_{eff} obtained using different methods.

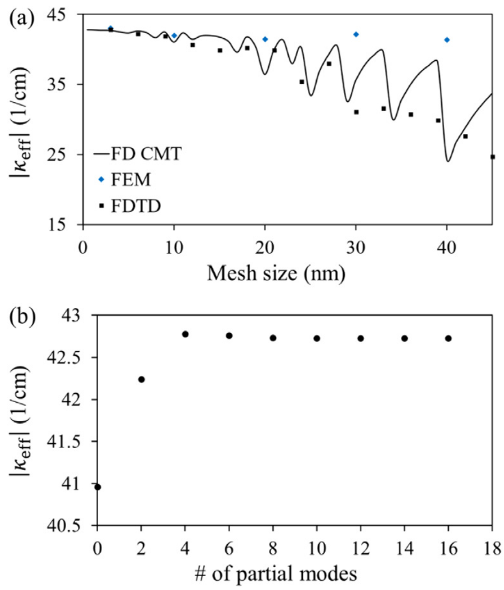

Fig. 6. (a) Coupling coefficient $|\kappa_{\mathrm{eff}}|$ as a function of the mesh size used in FD CMT, FEM, and FDTD. (b) $|\kappa_{\mathrm{eff}}|$ as a function of the number of partial modes included in the FD CMT.

waves, so no radiation loss occurs in this case. This minimizes the threshold current and maximizes the slope efficiency, but it makes the laser susceptible to mode hopping due to the degeneracy of the longitudinal modes. In a DFBL with a higher-order grating, the radiation loss associated with the resonant coupling between guided and partial waves increases the threshold current and reduces the slope efficiency, but it has the advantage of breaking longitudinal mode degeneracy [22–25]. To demonstrate the mode selectivity in higher-order gratings, we optimize a fifth-order grating in this section for the single-mode operation. We chose a fifth-order grating for three reasons: first, while second- and third-order gratings have been extensively studied [8,9,23,25,26] and fourth-order to some extent [27,28], fifth-order gratings remain relatively unexplored. Second, in the O-band, a fifth-order grating has a pitch of $\sim$1 µm, which is well-suited for fabrication using inexpensive photolithography techniques, e.g., based on a mask aligner. Third, fifth-order gratings inherently have many radiative modes, making them good candidates to test the accuracy of our FD CMT scheme.

Table 3 describes the parameters of the model structure depicted in Fig. 1 used for an illustration of how the WBG could be optimized for a single-mode DFBL operation. It is representative of an InP-based DFBL with the overgrown WBG. By varying the values of w and d $(= d_1 = d_2)$, the trapezoid grating profile may be changed to rectangular or triangular. Varying g adjusts the depth of the grating. The optimization procedure is as follows: we vary w from 0 to 1 (in a step size of 0.02) and d from 0 to $(1 - w)/2$ (in a step size of 0.02). Increasing d further will make the groove profile resemble an outward trapezoid, which is unlikely to occur in fabrication. Therefore, we excluded such cases from our analysis.

We vary g from 0.25 to 0.75 µm in a step of 0.25 µm. The optimization goal for such a structure is to achieve a single-mode spectrum while maintaining a high coupling coefficient magnitude. The coupling strength of a grating is commonly assessed

Table 3. Parameters of the Grating System 2

Parameter	n_1	n_2	n_3	P	b	λ_B
Value	3.2	3.3	3.2	5	1 µm	1300 nm

using the product of the coupling coefficient and the length, denoted $|\kappa_{\mathrm{eff}}|L$. A strong grating is characterized by $|\kappa_{\mathrm{eff}}|L > 1$, indicating that for a typical laser length of 1 mm, the value of $|\kappa_{\mathrm{eff}}|$ should be at least $10\ \mathrm{cm}^{-1}$. Thus, in our optimization algorithm, we assume a 1 mm long laser and only consider the geometries that result in $|\kappa_{\mathrm{eff}}|$ values greater than $10\ \mathrm{cm}^{-1}$. We select the one with the largest phase from the resulting geometries to achieve single-mode performance.

Figures 7(a) and 7(b) depict the amplitude and phase, respectively, of the coupling coefficient at a wavelength of 1300 nm computed using the algorithm discussed in Section 2.A. The data points with $|\kappa_{\mathrm{eff}}| < 10\ \mathrm{cm}^{-1}$ are omitted for clarity. The simulation was conducted with the following settings: $X_{\min} = -3$ µm, $X_{\max} = 3$ µm, $-7 < q < 7$, and a step size of 3 nm for the discretization.

Upon initial observation, it is evident that the amplitude peaks coincide with minima in phase, and conversely, minimum amplitudes correspond to larger phase values. Deeper gratings generally exhibit higher amplitude and phase. It is important to note that the selection of groove shapes should be tailored to the specific application, as different applications may require different characteristics. However, in our case, we prioritize gratings with the largest phase.

Radiating waves interact with the contradirectional guided waves in a grating structure, partially coupling back into the laser waveguide. This interaction decreases or increases the guided wave intensity, effectively inducing additional loss or gain to the guided wave. From Fig. 7(b), we see that the sign of the phase of the coupling coefficient depends on the grooves' profile and can be either positive or negative, corresponding to partial gain or loss coupling, respectively. To achieve natural single-mode behavior in DFBLs, it is desirable to have a phase of large magnitude. According to Fig. 7(b), the largest phase is achieved at $w = 0.04$, $d = 0.32$, and $g = 0.75$ µm, corresponding to our optimized design.

To evaluate the lasing condition of the WBGs, we need to solve the coupled wave equations for the forward R and backward S traveling waves [11]:

$$\frac{dR}{dz} - (\alpha + i\delta + i\zeta_1)R = i\left(\kappa_p^* + \zeta_2\right) S, \tag{18a}$$

$$-\frac{dS}{dz} - (\alpha + i\delta + i\zeta_1)S = i\left(\kappa_p + \zeta_4\right) R, \tag{18b}$$

where $\delta = \beta - \beta_0$ represents the Bragg detuning parameter and α represents the sources of loss and gain, expressed as

$$\alpha = \Gamma g_{\mathrm{mat}} - \alpha_{\mathrm{sca}} - \alpha_{\mathrm{abs}}, \tag{19}$$

where α_{abs} denotes the mode's loss due to material absorption, here assumed to be 0. The term α_{sca} refers to the scattered loss, represented by the normalized radiated power of partial waves escaping from the cavity and dissipating in the cover and substrate regions [6]:

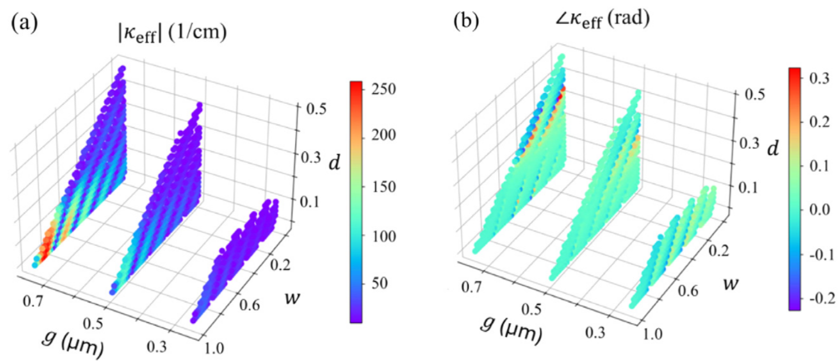

Fig. 7. (a) Amplitude and (b) phase of the effective coupling coefficient, κ_{eff}, as a function of d, w, and g.

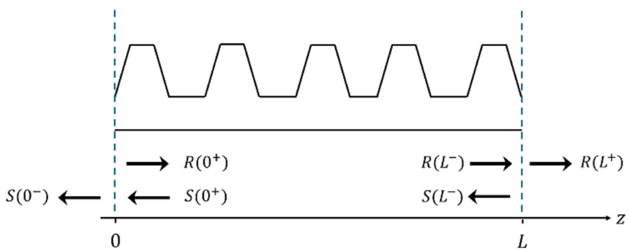

Fig. 8. Schematic of a DFB longitudinal cross section with forward R and backward S traveling waves.

$$\alpha_{\mathrm{sca}} = \sum_m \mathrm{Re}\left\{\sqrt{k_0^2 n_c^2 - \beta_m^2}|\varepsilon_m(0)|^2 + \sqrt{k_0^2 n_s^2 - \beta_m^2}|\varepsilon_m(b)|^2\right\}$$
$$/\left(\beta_0 \int_{-\infty}^{\infty} |\varepsilon_0(x)|^2 \mathrm{d}x\right). \quad \textbf{(20)}$$

For our optimized structure, α_{sca} is $8.14\ \mathrm{cm}^{-1}$. The term Γg_{mat} represents the modal gain, where Γ is the fraction of mode power overlapping with the gain region and g_{mat} is the material gain. The parameters α and δ are inherently coupled and typically solved numerically as pairs. We find these pairs numerically, based on the formulation discussed in Ref. [29]. To do so, we first define our boundary conditions. In our DFB structure, we assume that the facets at $z = 0$ and $z = L$ are cleaved and have the reflectivity of r, i.e., $R(0^+) = r\,S(0^+)$ and $S(L^-) = r\,R(L^-)$, as illustrated in Fig. 8. Figure 9 presents the paired eigenvalues, δ and α, at $L = 1$ mm and $r = 0.28$ (which is a typical value for an air/III–V material interface). These eigenvalue pairs determine the threshold characteristics of all potential lasing modes.

From Fig. 9, the shorter wavelength side of λ_B (right side of $\delta = 0$) exhibits the lowest threshold gain ($\alpha_{\mathrm{th}} = 1.23\ \mathrm{cm}^{-1}$), indicating it is the lasing mode. This notable disparity in threshold gain between this mode and its adjacent modes ensures a pronounced single-mode behavior and effective suppression of side modes. By substituting this value into Eq. (19), we find that this laser requires a modal gain Γg_{mat} of $9.37\ \mathrm{cm}^{-1}$ to reach the threshold gain. g_{mat} depends on the material system of the active region and the carrier injection level. For a typical III–V gain medium with multiple quantum wells, g_{mat} can reach values beyond $1000\ \mathrm{cm}^{-1}$. Γ is highly dependent on the waveguide geometry and typically is around 0.1 [30,31].

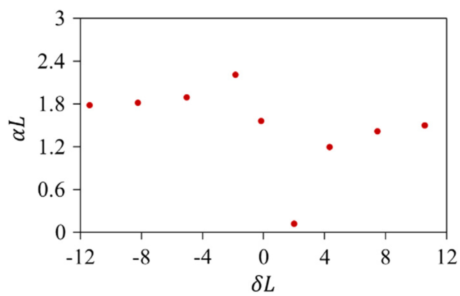

Fig. 9. Threshold characteristics of all potential lasing modes of System 2 for a cavity length of $L = 1$ mm and $r = 0.28$.

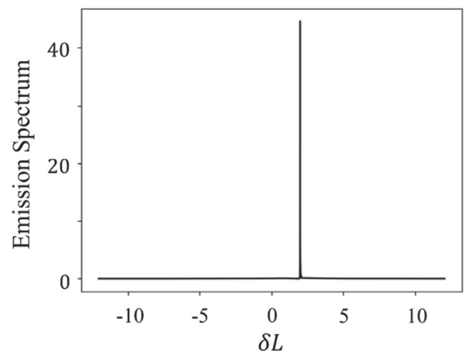

Fig. 10. Subthreshold emission spectrum of the optimized DFB structure with a groove profile defined by $w = 0.04$, $d = 0.32$, and $g = 0.75$ μm.

Figure 10 presents the emission spectrum derived using the analytic method described in Ref. [32], with α being just below the α_{th}. The spectrum reveals a pronounced natural single-mode behavior at $\delta L \approx 2$, consistent with the observations in Fig. 9.

5. CONCLUSION

We developed a semi-numerical algorithm based on the previously established coupled-mode theory to investigate waveguide gratings. We achieved excellent agreement with other numerical methods offered by commercial software packages. Our approach exhibits significantly faster computational performance, making it suitable for optimizing devices with extensive parameter sweeps. Leveraging this method, we investigated a generic InP-based grating and optimized it for single-mode

DFB operation, which is crucial for applications that demand a stable and high-quality signal output. The optimization, involving over 2000 different geometries using the FD CMT, would have been impractical to complete within a comparable timeframe using the FEM or FDTD.

Disclosures. The authors declare no conflicts of interest.

Data availability. Data underlying the results presented in this paper are not publicly available at this time but may be obtained from the authors upon reasonable request.

REFERENCES

1. L. A. Coldren, P. A. Verrinder, and J. Klamkin, "A review of photonic systems-on-chip enabled by widely tunable lasers," IEEE J. Quantum Electron. **58**, 6300110 (2022).
2. K. A. Williams, E. A. J. M. Bente, D. Heiss, *et al.*, "InP photonic circuits using generic integration," Photonics Res. **3**, B60–B68 (2015).
3. M. J. R. Heck, J. F. Bauters, M. L. Davenport, *et al.*, "Ultra-low loss waveguide platform and its integration with silicon photonics," Laser Photonics Rev. **8**, B60–B68 (2014).
4. H. Kogelnik and C. V. Shank, "Coupled-wave theory of distributed feedback lasers," J. Appl. Phys. **43**, 2327–2335 (1972).
5. A. Yariv, "Coupled-mode theory for guided-wave optics," IEEE J. Quantum Electron. **9**, 919–933 (1973).
6. W. Streifer, D. R. Scifres, and R. D. Burnham, "Analysis of grating-coupled radiation in GaAs:GaAlAs lasers and waveguides-I," IEEE J. Quantum Electron. **12**, 422–428 (1976).
7. J. Ctyroký, S. Helfert, R. Pregla, *et al.*, "Bragg waveguide grating as a 1D photonic band gap structure: COST 268 modelling task," Opt. Quantum Electron. **34**, 455–470 (2002).
8. H. Wenzel, R. Guther, A. M. Shams-Zadeh-Amiri, *et al.*, "A comparative study of higher order Bragg gratings: coupled-mode theory versus mode expansion modeling," IEEE J. Quantum Electron. **42**, 64–70 (2005).
9. R. R. Millet, K. Hinzer, T. J. Hall, *et al.*, "Simulation analysis of higher order laterally-coupled distributed feedback lasers," IEEE J. Quantum Electron. **44**, 1145–1151 (2008).
10. KVector, "Dynamics Grating Solver," https://kvectordynamics.com/grating-solvers/.
11. W. Streifer, D. R. Scifres, and R. D. Burnham, "Coupled wave analysis of DFB and DBR lasers," IEEE J. Quantum Electron. **13**, 134–141 (1977).
12. J. P. Donnelly and S. D. Lau, "Generalized effective index series solution analysis of waveguide structures with positionally varying refractive index profiles," IEEE J. Quantum Electron. **32**, 1070–1079 (1996).
13. L. Shen and Z. Wang, "Guided modes in a four-layer slab waveguide with dispersive left-handed material," J. Electromagn. Anal. Appl. **2**, 264–269 (2010).
14. C. H. Chen, L. H. Chen, and Q. M. Wang, "Coupling coefficients of gain-coupled distributed feedback lasers with absorptive grating," Electron. Lett. **32**, 1288–1290 (1996).
15. COMSOL Multiphysics, https://www.comsol.com/.
16. A. Taflove, A. Oskooi, and S. G. Johnson, *Advances in FDTD Computational Electrodynamics: Photonics and Nanotechnology* (Artech House, 2013).
17. D. C. Flanders, H. Kogelnik, R. V. Schmidt, *et al.*, "Grating filters for thin-film optical waveguides," Appl. Phys. Lett. **24**, 194–196 (1974).
18. W. Sun, Q. Lu, W. Guo, *et al.*, "Analysis of high-order slotted surface gratings by the 2D finite-difference time-domain method," J. Lightwave Technol. **35**, 96–102 (2016).
19. S. Saeidi, F. Wu, C. Watson, *et al.*, "Strong and short Bragg waveguide gratings with trapezoidal-shaped grooves," J. Lightwave Technol. **39**, 4395–4401 (2021).
20. X. Wang, Y. Wang, J. Flueckiger, *et al.*, "Precise control of the coupling coefficient through destructive interference in silicon waveguide Bragg gratings," Opt. Lett. **39**, 5519–5522 (2014).
21. "Lumerical is now part of the Ansys family," 2023, https://www.lumerical.com/.
22. T. Makino and J. Glinski, "Effects of radiation loss on the performance of second-order DFB semiconductor lasers," IEEE J. Quantum Electron. **24**, 73–82 (1988).
23. R. Kazarinov and C. Henry, "Second-order distributed feedback lasers with mode selection provided by first-order radiation losses," IEEE J. Quantum Electron. **21**, 144–150 (1985).
24. V. Tolstikhin, C. Watson, K. Pimenov, *et al.*, "Laterally coupled DFB lasers for one-step growth photonic integrated circuits in InP," IEEE Photonics Technol. Lett. **21**, 621–623 (2009).
25. K. Pimenov, C. Watson, Y. Logvin, *et al.*, "Analysis of high-order surface etched gratings for longitudinal mode selection in DFB lasers," in *Numerical Simulation of Optoelectronic Devices* (2010), pp. 49–50.
26. L. Zhang and D. A. Ackerman, "Second- and third-order harmonic distortion in DFB lasers," IEEE J. Quantum Electron. **31**, 1974–1980 (1995).
27. J. Kinoshita, "Analysis of radiation mode effects on oscillating properties of DFB lasers," IEEE J. Quantum Electron. **35**, 1569–1583 (1999).
28. A. Akrout, K. Dridi, and T. J. Hall, "Dynamic analysis of high-order laterally coupled DFB lasers using time-domain traveling-wave model," IEEE J. Quantum Electron. **48**, 1252–1258 (2012).
29. G. P. Agrawal and N. K. Dutta, *Semiconductor Lasers* (Van Norstrand Reinhold, 1993).
30. S. R. Selmic, T.-M. Chou, J. Sih, *et al.*, "Design and characterization of 1.3-/spl mu/m AlGaInAs-InP multiple-quantum-well lasers," IEEE J. Sel. Top. Quantum Electron. **7**, 340–349 (2001).
31. J. Piprek, P. Abraham, and J. E. Bowers, "Self-consistent analysis of high-temperature effects on strained-layer multiquantum-well InGaAsP-InP lasers," IEEE J. Quantum Electron. **36**, 366–374 (2000).
32. T. Makino and J. Glinski, "Transfer matrix analysis of the amplified spontaneous emission of DFB semiconductor laser amplifiers," IEEE J. Quantum Electron. **24**, 1507–1518 (1988).